



1 **Extreme Weather exacerbates Ozone Pollution in the Pearl**  
2 **River Delta, China: Role of Natural Processes**

3 Nan Wang<sup>1</sup>, Hongyue Wang<sup>2</sup>, Xin Huang<sup>3</sup>, Xi Chen<sup>4</sup>, Xiaopu Lyu<sup>5\*</sup>, Yu  
4 Zou<sup>6</sup>, Tao Deng<sup>6</sup>, Tingyuan Li<sup>7</sup>, Fumo Yang<sup>1\*</sup>

5

6 <sup>1</sup>College of Carbon Neutrality Future Technology, Sichuan University, Sichuan, China

7 <sup>2</sup>Department of Atmospheric Science, China University of Geosciences, Wuhan,  
8 430078, China

9 <sup>3</sup>School of Atmospheric Science, Nanjing University, Nanjing, China

10 <sup>4</sup>Institute of Mass Spectrometry and Atmospheric Environment, Guangdong  
11 Provincial Engineering Research Center for On-line Source Apportionment System of  
12 Air Pollution, Jinan University, Guangzhou, PR China

13 <sup>5</sup>Department of Geography, Hong Kong Baptist University, Hong Kong, 000000,  
14 China

15 <sup>6</sup>Institute of Tropical and Marine Meteorology, China Meteorological Administration  
16 (CMA), Guangzhou, China

17 <sup>7</sup>Guangdong Ecological Meteorological Center, Guangzhou, China

18 Correspondence to xiaopu\_lyu@hkbu.edu.hk and fmyang@scu.edu.cn

19

20

21 **KEYWORDS:** ozone pollution, extreme weather, natural process, BVOC

22 emission, STE

23



24

## Abstract

25 Ozone (O<sub>3</sub>) pollution research and management in China have mainly  
26 focused on anthropogenic emissions, while the importance of natural  
27 processes is often overlooked. With the increasing frequency of extreme  
28 weather events, the role of natural processes in exacerbating O<sub>3</sub> pollution  
29 is gaining attention. In September 2022, the Pearl River Delta (PRD) in  
30 South China experienced an extended period (25 days) of regional O<sub>3</sub>  
31 exceedances and high temperatures (2<sup>nd</sup> highest over last 2 decades) due to  
32 extreme weather conditions influenced by the Subtropical High and  
33 typhoon peripheries. Employing an integrated approach involving field  
34 measurements, machine learning, and numerical model simulations, we  
35 investigated the impact of weather-induced natural processes on O<sub>3</sub>  
36 pollution by considering meteorological factors, natural emissions,  
37 chemistry pathways, and atmospheric transport. It was found that the hot  
38 weather significantly promoted regional photochemical reactions, with  
39 meteorological factors contributing to an additional 10.8 ppb of O<sub>3</sub> levels  
40 compared to normal conditions. Temperature was identified as the  
41 dominant factor influencing O<sub>3</sub> pollution. The hot weather also intensified  
42 the emission of biogenic volatile organic compounds by ~10%. Notably,  
43 isoprene and biogenic formaldehyde accounted for about half of the in-situ  
44 O<sub>3</sub> production. The chemical mechanism of isoprene contributing to O<sub>3</sub>  
45 formation was further explored, with O<sub>3</sub> production more attributable to  
46 the further degradation of early generation isoprene oxidation products  
47 than the direct isoprene oxidation itself. Furthermore, the typhoon nearing  
48 landfall significantly enhanced the cross-regional transport of O<sub>3</sub> from  
49 northern to southern China through stratosphere-to-troposphere exchange  
50 (STE). The CAM-Chem model simulations revealed that the STE-induced  
51 O<sub>3</sub> on the PRD surface could reach a maximum of ~ 8 ppb, highlighting  
52 the non-negligible impact of STE. This study highlights the importance of  
53 natural processes exacerbated by extreme weather events in O<sub>3</sub> pollution  
54 and provides valuable insights for O<sub>3</sub> pollution control under global  
55 warming.



## 56 **1 Introduction**

57 Ground-level ozone ( $O_3$ ) is a secondary air pollutant with adverse effects  
58 on human health, vegetation, crop yields, and climate (Knowlton et al.,  
59 2004; Ashmore, 2005; Eyring et al., 2013). The formation of tropospheric  
60  $O_3$  is a result of sun-light driven photochemical reactions involving  
61 nitrogen oxides ( $NO_x$ ), volatile organic compounds (VOC), and other  
62 pollutants (Derwent et al., 1998; Jacob, 2000). The relationship between  
63  $O_3$  and its precursors exhibits a non-linear pattern that varies across  
64 different regions (Jenkin and Clemitshaw, 2000).  $O_3$  and its precursors  
65 originate from both anthropogenic activities and natural processes such as  
66 fossil fuel combustion, biogenic volatile carbon (BVOC) emissions and  
67 stratosphere-troposphere exchange (STE). Meteorological conditions also  
68 play a crucial role in influencing  $O_3$  pollution, adding complexity to  
69 mitigation efforts (Wang et al., 2017).

70 Since the industrial revolution, the northern hemisphere has experienced a  
71 significant increase in  $O_3$  pollution, particularly in mid-latitude cities with  
72 large populations and industries (Gaudel et al., 2018). In recent decades,  
73 Europe and the United States have made notable progress in mitigating  $O_3$   
74 pollution through emission control efforts. However, eastern Asia, notably  
75 China, continues to face a severe  $O_3$  pollution problem. Despite the  
76 implementation of strict emission control measures, such as the Air  
77 Pollution Prevention and Control Action Plan and the reduction in fine  
78 particulate matter concentrations,  $O_3$  levels in China have continued to rise  
79 (Wang et al., 2019). Lu et al. (2018) reported that  $O_3$  pollution days in  
80 China are 93 to 575% higher compared to other developed countries,  
81 indicating the significant public concern surrounding this issue.

82 Despite human activities being recognized as major contributors to severe  
83  $O_3$  pollution, it is also important to acknowledge the role of meteorological  
84 conditions on the dynamics of tropospheric  $O_3$  concentrations. For example,  
85 temperature has a direct impact on chemical reaction rates involved in  $O_3$   
86 formation as well as the emissions of biogenic volatile organic compounds  
87 (BVOCs) from vegetation (Lu et al., 2019). Atmospheric water vapor, on  
88 the other hand, plays a crucial role by providing  $HO_x$  radicals and directly  
89 influencing  $O_3$  photochemistry (Camalier et al., 2007). Additionally, wind



90 patterns contribute to the transport and dispersion of pollutants, thereby  
91 influencing the spatial distribution of O<sub>3</sub> and its precursors (Wang et al.,  
92 2022). Nonetheless, the local meteorological parameters are controlled by  
93 synoptic weather system. Generally, the role of weather systems manifests  
94 in two aspects, one is via the influence on the regional transport of  
95 pollutants, and the other is modulating the aggregation and dispersion of  
96 local air pollutants (Ding et al., 2017). Extensive research conducted in  
97 eastern China has shed light on the importance of weather patterns and  
98 addressed on the impact of extreme weather contributing to O<sub>3</sub> pollution.  
99 Notably, anticyclones (such as high-pressure systems) and the periphery of  
100 typhoons have emerged as prominent factors (Chan and Chan, 2000; Han  
101 et al., 2020; Gao et al., 2021). Besides, nature processes, including the  
102 natural sources, chemistry and atmospheric transport of O<sub>3</sub>, are highly  
103 meteorology-sensitive and might further aggravate O<sub>3</sub> pollution under  
104 extreme weather. For example, the wildfire caused by hot and dry weather  
105 could emit large amount of CO, NO<sub>x</sub> and VOCs and exacerbate O<sub>3</sub>  
106 pollution (Westerling et al., 2006; Yue and Unger, 2018; Lei et al., 2022);  
107 Vegetation-released BVOCs emissions are sensitive to temperature and  
108 have been proven to increase during hot season and thus accelerate urban  
109 O<sub>3</sub> formation (Pusede et al., 2015; Wang et al., 2022); An STE event would  
110 bring stratospheric O<sub>3</sub> to the troposphere under a largescale/mesoscale  
111 process such as tropopause folds, gravity wave breaking, and deep  
112 convections (Stohl et al., 2003; Wang et al., 2020). As global warming  
113 progresses, there is an increase in the frequency of extreme weather events  
114 which further impact surface O<sub>3</sub> (Banerjee et al., 2016; Lu et al., 2019).  
115 These impacts may undermine or offset the efforts by anthropogenic  
116 emission reductions, posing risks to the ecological environment. Therefore,  
117 understanding the influence of natural process on the formation of ground-  
118 level O<sub>3</sub> is essential for gaining insights into the dynamics of O<sub>3</sub> pollution  
119 and developing effective strategies for managing air quality.  
120 The Pearl River Delta (PRD) region, known for its high levels of  
121 anthropogenic emissions and surrounded by significant vegetation cover,  
122 frequently suffers from extreme weather events such as heat waves and  
123 tropical cyclones. The PRD region has emerged as a typical hotspot



124 witnessing an increase in O<sub>3</sub> pollution, making it an ideal location to  
125 investigate the impact of extreme weather on O<sub>3</sub> pollution. In September  
126 2022, the PRD endured a prolonged period of hot weather, leading to more  
127 than 20 days of regional O<sub>3</sub> exceedance. Here, by integrating simultaneous  
128 measurements, machine learning, and numerical model simulations, we  
129 aim to improve the understanding of how natural processes induced by  
130 extreme weather events affecting O<sub>3</sub> pollution and provide new insights for  
131 future O<sub>3</sub> pollution control efforts.

## 132 **2 Methods and Materials**

### 133 **2.1 Data Source**

134 In-situ observations were conducted at the Guangzhou Haizhu Urban  
135 Ecological Meteorological Comprehensive Observation Base (HZ Base,  
136 23°05'N, 113°22'E), which is located in the North area of the Guangzhou  
137 Haizhu District National Wetland Park (as shown in Figure 1a). The  
138 observation base is surrounded by basic farmland protection areas and  
139 represents a typical composite wetland system consisting of river channels,  
140 creeks, fruit orchards, and the Jiangxinzhou Island. It also encompasses  
141 commercial streets, residential areas, and major transportation routes,  
142 providing a representation of wetland climate and human activities.  
143 Synchronous online observations of O<sub>3</sub>, NO<sub>x</sub>, SO<sub>2</sub>, CO, components of  
144 VOCs, and meteorological parameters (surface winds, temperature and  
145 solar radiation) were carried out at this observation base. Detailed  
146 information about the data used, including the monitoring instruments, data  
147 coverage, and access method, was summarized in Table S1. Briefly,  
148 ambient concentrations of O<sub>3</sub>, NO<sub>x</sub>, CO and SO<sub>2</sub> were routinely measured  
149 using instruments produced by Thermo Scientific (49i-D1NAA, 42i-  
150 DNMSDAA, 48i-DNSAA and 43i-DNSAA, respectively). The species of  
151 VOC components were monitored by GC5000 analysis systems coupled  
152 with flame ionization detectors (FID) from AMA Instruments GmbH  
153 (AMA, Germany). All instruments were regularly calibrated and  
154 maintained for different durations. Meteorological data, including  
155 temperature, solar radiation, precipitation, relative humidity and winds,  
156 were obtained at the same site from the China Meteorological  
157 Administration. The in-situ measurements were mainly used to drive a



158 photochemical box model as described below. Additionally, the air quality  
159 monitoring network established by the Ministry of Ecology and  
160 Environment of China was utilized to identify O<sub>3</sub> pollution event in PRD.  
161 There were 56 monitoring site distributed in the whole region (Figure 1a)  
162 and the 90th percentile of the maximum daily 8-hour average (MDA8-90)  
163 O<sub>3</sub> concentration was employed to assess the regional degree of O<sub>3</sub>  
164 pollution.

165 In addition to the in-situ data, ancillary data from the fifth generation of the  
166 European Centre for Medium-Range Weather Forecasts atmospheric  
167 reanalysis (ERA5) were utilized. The ERA5 data, at a resolution of 0.25°  
168 × 0.25° grid, corresponded to the same time period and interval as the  
169 observed data and provided information such as boundary layer height,  
170 potential vorticity, vertical velocity, geopotential height, specific humidity  
171 and O<sub>3</sub> mass mixing ratio. Besides, typhoon tracks occurred in West Pacific  
172 Ocean were collected from China Meteorology Administration Tropical  
173 Cyclone Data Center (<https://tcdata.typhoon.org.cn>).

## 174 **2.2 Stepwise Regression Analysis**

175 The stepwise regression analysis, as a common method of machine  
176 learning, was used to simulate the dynamics of O<sub>3</sub> concentrations and  
177 quantitatively assess the influence of various meteorological factors on  
178 pollutant variations. The method was designed to construct an optimal  
179 equation by iteratively selecting significant factors while eliminating non-  
180 significant ones to address autocorrelation concerns (Johnsson, 1992). In  
181 this study, simple regressions were firstly performed for each explanatory  
182 variable, and the variable with the most significant contribution was  
183 identified. Subsequently, additional variables were gradually introduced,  
184 and the F-test and t-test were employed to evaluate their significance. Non-  
185 significant variables were progressively eliminated until we obtained a  
186 final set of critical explanatory variables. Following variable selection, a  
187 multivariate linear regression equation was established to capture the  
188 variation of O<sub>3</sub> concentrations:

$$189 \quad O_3(t) = \alpha \text{VAR}_1(t) + \beta \text{VAR}_2(t) + \gamma \text{VAR}_3(t) + \dots + \eta \text{VAR}_n(t) + R(t) \quad (1)$$

190 In Eq. (1), O<sub>3</sub>(t) represents the temporal changes in O<sub>3</sub> concentration at  
191 hour t. The coefficients (α, β, γ, η) for each variable (VAR) were



192 determined during the stepwise regression process, while  $R(t)$  represents  
193 the residual error term. This approach enables us to effectively analyze the  
194 intricate relationship between meteorological factors and  $O_3$   
195 concentrations, providing valuable insights into the dynamics of  $O_3$   
196 pollution. This utilized approach has proven effective in our previous  
197 pollutant simulations (Chen et al., 2022). In this study, the model's  
198 performance was validated through Figure S1, demonstrating a strong  
199 correlation ( $R > 0.84$  and  $P < 0.01$ ) between the observed and simulated  $O_3$   
200 concentrations.

### 201 **2.3 Lagrangian Dispersion Modeling**

202 We conducted backward Lagrangian particulate dispersion modeling  
203 (LPDM) using the Hybrid Single-Particulate Lagrangian Integrated  
204 Trajectory model (HYSPLIT) to identify the dominant air flow impacting  
205 the receptor area. The meteorology fields were from the Global Data  
206 Assimilation System (GDAS) data. In this study, we released 3000  
207 particulates at 100 m above sea level (a.s.l) over the site (HZ Base) and  
208 tracked their backward movement for 48 hours with a time resolution of 1  
209 hour. The positions of the particulates were determined using both vertical  
210 and horizontal calculations, considering mean wind and turbulence  
211 transport. The model finally identified the "retroplume" footprint  
212 representing the spatial residence time of the particulates and could be  
213 regarded as the distribution of the simulated air mass's surface probability  
214 or residence time.

### 215 **2.4 MEGAN model**

216 The Model of Emissions of Gases and Aerosols from Nature (MEGAN,  
217 version 2.1) was used to estimate BVOC emissions from terrestrial  
218 ecosystems (Guenther et al. (2012)). The model could calculate 147  
219 individual biogenic compounds and lump them into the appropriate VOC  
220 mechanisms such as CB05, RACM, SAPRC99 and etc. Herein, the CB05  
221 mechanism was adopted for VOC treatment. Due to the versatility and  
222 compatibility, the MEGAN model could be incorporated into many widely  
223 used chemical transport models with horizontal resolution ranging from a  
224 few kilometers to several hundred kilometers. In this study, the plant  
225 function type (PFT) data was from MODIS (Moderate-Resolution Imaging



226 Spectroradiometer) MCD12Q1 product and the leaf area index (LAI) data  
227 was from MODIS MCD15A2H product. The input meteorology including  
228 temperature, solar radiation, and relative humidity was obtained from  
229 WRF-CMAQ (Weather Research Forecast-Community Multi Scale Air  
230 Quality) simulations with a horizontal resolution of  $12\text{km} \times 12\text{km}$ . The  
231 configuration of the model was summarized in Table S2. In particular, to  
232 emphasize the influence of extreme weather, comparisons of BVOCs  
233 emissions from parallel simulations were conducted. In detail, we  
234 employed two sets of meteorological fields to drive the MEGAN model,  
235 respectively. One set was based on the WRF-simulated meteorology from  
236 September 2022, while the other utilized the average meteorological fields  
237 from the preceding three years (2019-2021).

### 238 **2.5 In-situ photochemistry modeling**

239 In-situ  $\text{O}_3$  formation was simulated using the Framework for 0-D  
240 Atmospheric Modeling (F0AM) incorporating Master Chemical  
241 Mechanism v3.3.1. The application method was roughly in line with that  
242 in (Lyu et al., 2022). Briefly, the model was constrained by observations  
243 including  $\text{O}_3$ ,  $\text{NO}_x$ , CO,  $\text{SO}_2$ , VOCs species and meteorological parameters  
244 collected at HZ Base at hourly resolution. Specifically, HCHO was not  
245 measured and was constrained by the WRF-CMAQ simulation results (The  
246 validation of WRF-CMAQ was summarized in Table S3). A ‘family  
247 conservation’ that set the total  $\text{NO}_x$  to the observed value every hour and  
248 allowed NO and  $\text{NO}_2$  to evolve over time was applied (Wolfe et al., 2016).  
249 Photolysis frequency of  $\text{NO}_2$  observed at HZ Base was input and used to  
250 correct the photolysis frequencies of other species. Net  $\text{O}_3$  production rate  
251 (OPR) was calculated as the difference between  $\text{O}_3$  production rate ( $\text{NO}_2$   
252 production through NO oxidation by peroxy radicals) and destruction rate  
253 ( $\text{NO}_2$  reacting with OH,  $\text{O}_3$  photolysis, ozonolysis of alkenes, and  $\text{O}_3$   
254 consumption by OH and  $\text{HO}_2$ ), in line with the way adopted in previous  
255 studies (Lyu et al., 2019; Wang et al., 2017). The reaction rates for a total  
256 of 17,224 reactions were exacted to diagnose the main isoprene-related  
257 pathways leading to  $\text{O}_3$  formation.

258  
259





## 260           **2.6 CAM-Chem model**

261   The CAM-Chem (Chemical Lagrangian Model of the Stratosphere), a  
262   component of the NCAR Community Earth System Model (CESM)  
263   version 2.2.0, was utilized to simulate the impact of stratosphere-to-  
264   troposphere exchange (STE) transported O<sub>3</sub> on the troposphere. The  
265   meteorological fields were obtained from MERRA2 and regridded to a 32-  
266   vertical layer with a horizontal resolution of 0.9×1.25°. The chemistry  
267   mechanism employed was the MOZART-T1. Further information about the  
268   model can be found in the CAM-Chem Wiki  
269   (<https://wiki.ucar.edu/display/camchem>). To validate the model's  
270   performance, we compared the distribution of the simulated O<sub>3</sub> with O<sub>3</sub>  
271   from AIRS (Atmospheric Infrared Sounder). Both the monthly averaged  
272   distribution and an STE-induced O<sub>3</sub> intrusion case were compared (Figure  
273   S2). Although the CAM-Chem simulations showed slightly higher O<sub>3</sub>  
274   levels in southern China, it was worth noting that the satellite retrievals  
275   themselves contain uncertainties, mainly from the impact of clouds,  
276   aerosols, surface albedo and the inversion algorithms. Overall, the  
277   simulated O<sub>3</sub> showed good agreement with the AIRS data in terms of  
278   magnitude and spatial pattern, indicating satisfactory model performances.  
279   Furthermore, a comparison of the CAM-Chem simulated ground-level O<sub>3</sub>  
280   with the surface network monitoring was also conducted (Figure S3). The  
281   daily magnitude and variation trend were successfully captured in  
282   Guangzhou, with a mean bias error (MBE) of -7.9 ppb and a root mean  
283   square error (RMSE) of 16.3 ppb. This demonstrated a good reproduction  
284   of surface O<sub>3</sub> concentrations. Indeed, our previous paper have also shown  
285   the good performance of the CAM-Chem model application in eastern  
286   China (Wang et al., 2023).

## 287           **3 Results and discussion**

### 288           **3.1 Exacerbation of O<sub>3</sub> Pollution due to Extreme Weather** 289           **Conditions**

290   In September 2022, the PRD region experienced continuous extreme  
291   weather, resulting in a prolonged period of hot weather conditions. As a  
292   consequence, the region encountered 25 consecutive days of regional O<sub>3</sub>  
293   pollution (Figure 1b). Monthly O<sub>3</sub> concentration (MDA8-90 O<sub>3</sub>) were



294 situated in high levels reaching up to 92 ppb, approximately 20 ppb higher  
295 than the average of the same period during past three years. Meanwhile,  
296 the monthly average daily-maximum temperature soared to 32°C, making  
297 it the second-highest temperature recorded in September over the past 2  
298 decades (Figure S4). The extremely high temperature appeared to be a  
299 significant driver of O<sub>3</sub> pollution, as evidenced by a high correlation  
300 coefficient of 0.70 ( $p < 0.05$ ) between O<sub>3</sub> levels and air temperature (Figure  
301 1b). From a synoptic weather perspective, the occurrence of hot weather  
302 was the combined effect of multiple tropical cyclones and Western Pacific  
303 Subtropical High (WPSH) (Figure 1c). It was recorded that there were four  
304 tropical cyclones within the one-month time (2022 September) influenced  
305 PRD (described in Table S4). As shown in Figure 1c, the combined effects  
306 of tropical cyclones and WPSH resulted in the splitting of the subtropical  
307 high into two parts. One part lingered over the western Pacific Ocean,  
308 while the other remained over the southern region of China, leaving the  
309 PRD under the fully control of the mainland high-pressure system.  
310 Affected by the sinking air flow under the mainland high, the PRD region  
311 experienced conditions characterized by high temperatures, intense solar  
312 radiation, low humidity, and reduced precipitation, creating a favorable  
313 environment for photochemical pollution (Figure 1d).

314 To assess the influence of meteorological parameters on O<sub>3</sub> concentrations,  
315 we developed a stepwise regression model to simulate regional O<sub>3</sub>  
316 concentrations. By incorporating an extensive range of input variables,  
317 including surface and 850hPa meteorological factors, we rigorously tested  
318 and identified ten significant factors through T-test analysis. These factors  
319 comprised the following: 2m temperature (T2), boundary layer height  
320 (BLH), surface relative humidity (RH), surface wind speed (WS), 10m U-  
321 component of wind (U10), vertical wind speed (W), 850hPa U-component  
322 of wind (U850), total cloud coverage (TCC), 10m V-component of wind  
323 (V10), and 850hPa V-component of wind (V850). As illustrated in Figure  
324 2, meteorological parameters exerted a crucial influence on O<sub>3</sub>  
325 concentrations in 2022, surpassing levels in previous years (2019-2021).  
326 This underscored the profound impact of meteorology on O<sub>3</sub> pollution.  
327 Notably, the factor associated with photochemistry, such as T2, BLH, and



328 RH, played a substantial role, contributing 43.1 ppb, 35.7 ppb, and -9.3 ppb,  
329 respectively, to the overall O<sub>3</sub> concentration. In particular, the average  
330 daily-maximum air temperature in September maintained at a typically  
331 high level (32 °C), which not only accelerated the rates of photochemical  
332 reactions, but also stimulated the emission of BVOCs from vegetation,  
333 thereby exacerbating O<sub>3</sub> concentrations. Furthermore, the increase in BLH  
334 and WS compared to previous years indicated relatively favorable  
335 ventilation conditions, which facilitated the transport of local and upstream  
336 pollutants. Subsequent investigations unveiled that air pollutants from  
337 northern regions could be transported to the PRD, contributing to the  
338 observed O<sub>3</sub> concentrations (refer to Section 3.3). Additionally, September  
339 exhibited relatively dry conditions with lower relative humidity (RH) and  
340 less precipitation. Our model revealed a negative correlation between O<sub>3</sub>  
341 and RH, suggesting that the presence of water vapor contributed to the  
342 photochemical removal of O<sub>3</sub> concentrations (e.g., through HO<sub>x</sub> reactions).  
343 The reduced RH in September also likely facilitated the persistence of O<sub>3</sub>  
344 pollution in the region.

345



### 3.2 Weather-boosted BVOC emissions aggravating O<sub>3</sub> production

346  
347 As one important precursor of O<sub>3</sub> formation, BVOC emissions are sensitive  
348 to ambient temperature and solar radiation. Here, we utilized MEGAN  
349 model to calculate the regional BVOC emissions. Parallel simulations  
350 driven by different meteorological inputs, i.e., meteorological fields in  
351 September 2022 and the average meteorological fields in September of the  
352 previous three years, were conducted, respectively. It was found that the  
353 hot weather in September 2022 led to an increase in BVOC emissions in  
354 the PRD region by approximately 10%, relative to that in the same period  
355 in the past (Figure 3a). Besides, the in-situ observed isoprene exhibited a  
356 significant concentration difference between day and night, i.e., 0.52 – 1.25  
357 ppb during 6:00 – 17:00 and an average of 0.10 ppb at other times. Not  
358 surprisingly, isoprene contributed 7.77 ppb h<sup>-1</sup> (~ 40%) to the in-situ net O<sub>3</sub>  
359 production rate (OPR) in daytime (Figure 3b). Nevertheless, this was likely  
360 a conservative estimate of the biogenic contributions, due to lack of  
361 consideration of other biogenic VOC. HCHO, as an important O<sub>3</sub> precursor,  
362 is of both anthropogenic and biogenic origin. Here, we utilized WRF-  
363 CMAQ simulated biogenic HCHO as input to examine its impact on O<sub>3</sub>  
364 formation with F0AM. It was found that biogenic HCHO at an average  
365 concentration of 2.46 ppb elevated the OPR by 1.29 ppb h<sup>-1</sup>. This increased  
366 the contribution to OPR of biogenic emissions to 47%. Overall, the  
367 modeling results underlined the crucial role of biogenic emissions in  
368 building up O<sub>3</sub> levels in September 2022.

369 Next, we explored the detailed mechanisms of O<sub>3</sub> formation enhancement  
370 induced by the rise in isoprene levels due to hot weather. Simulations were  
371 performed for a base case with observations in 2022 and a hypothetical  
372 case of lower isoprene levels. We used the ratio of isoprene emissions  
373 between 2022 and previous years to scale the observed isoprene in  
374 September 2022. So, isoprene in the base case was 10% higher than that in  
375 the hypothetical case. HCHO was constrained by the same profile in both  
376 cases. It was simulated that the 10% increase in isoprene would lead to an  
377 additional OPR of 1.00 ppb h<sup>-1</sup> at 12:00 when photochemical reactions  
378 were intense. While there was little change in the O<sub>3</sub> destruction pathways,  
379 the production of NO<sub>2</sub> through RO<sub>2</sub> + NO and HO<sub>2</sub> + NO (pathways



380 leading to O<sub>3</sub> formation following NO<sub>2</sub> photolysis) increased by 0.63 ppb  
381 h<sup>-1</sup> and 0.38 ppb h<sup>-1</sup>, respectively. As shown in Figure 4, this overall effect  
382 was caused by multiple reactions involving several generations of isoprene  
383 oxidation products/intermediates. The direct oxidation of isoprene by OH  
384 and the following transformation from RO<sub>2</sub> through RO to HO<sub>2</sub> only  
385 accounted for 30.3% and 42.8% of the increase in total rate of RO<sub>2</sub> + NO  
386 and HO<sub>2</sub> production, respectively. The rest was contributed by the  
387 degradation of methyl vinyl ketone (MVK) and methacrolein (MACR),  
388 two typical isoprene oxidation products (Pierotti et al., 1990). In particular,  
389 the formation of peroxyacetyl radical (CH<sub>3</sub>CO<sub>3</sub>) was enhanced by 0.16 ppb  
390 h<sup>-1</sup>, which further accelerated the rate of RO<sub>2</sub> oxidizing NO by 0.30 ppb h<sup>-1</sup>  
391 (45.6%) and HO<sub>2</sub> production rate by 0.15 ppb h<sup>-1</sup> (32.5%). Methylglyoxal  
392 (MGLYOX) and CH<sub>3</sub>CO<sub>3</sub> were the key intermediates in photochemical  
393 degradation of MVK and MACR that largely enhanced O<sub>3</sub> formation. The  
394 effect of MVK was much more significant than MACR, which was  
395 reasonable, due to the presence of a more reactive vinyl group in the MVK  
396 molecule.

397 It is well documented that isoprene emitted from vegetation is highly  
398 reactive in the troposphere and is therefore not prone to transport over long  
399 distances. Here, we show that the primary oxidation products of isoprene  
400 that may be formed during air mass transport (Wang et al., 2022),  
401 especially MVK and MACR, make significant contributions to O<sub>3</sub>  
402 formation. This presents to be an important mechanism of isoprene  
403 contributing to O<sub>3</sub> formation. Hence, the impacts of BVOC oxidation  
404 intermediates on downwind air quality warrant more attention.

### 405 **3.3 O<sub>3</sub> enhancement by STE and cross-regional transport**

406 In addition to its influence on meteorological factors and natural emissions,  
407 extreme weather can also impact atmospheric transport, modulating the  
408 regional air quality. For instance, the Stratosphere-Troposphere Exchange  
409 (STE) process is a significant natural process that facilitates the exchange  
410 of O<sub>3</sub>-rich air from the stratosphere to the troposphere, impacting O<sub>3</sub> levels  
411 in the lower atmosphere (Wang et al., 2023). STE often occurs in  
412 association with synoptic weather systems such as cyclones, westerly jet  
413 stream, frontal activities and troughs of low pressure (Banerjee et al., 2016).



414 Being affected by the combined influence of the Subtropical High and  
415 typhoons, we diagnosed a continuous STE event occurring from September  
416 13, 2022, to September 16, 2022.

417 Initially, on September 13, a trough of low pressure extended from  
418 northwest Inner Mongolia to central China, affecting a large portion of  
419 mainland China (Figure S5). Concurrently, Typhoon "Muifa" developed  
420 near the coastline in the western Pacific Ocean, leading to the gradual  
421 development of this trough towards the southeastern part of China. On the  
422 15th, the typhoon made landfall in the Yangtze River Delta region. The  
423 combined influence of the typhoon's low-pressure center and the external  
424 strong anticyclone further extended the trough of low pressure southward  
425 (Figure S5). The dynamic evolution of the weather system facilitated the  
426 favorable conditions for cross-regional transport from higher latitudes of  
427 China to the lower latitudes, such as the Pearl River Delta region.

428 Here, we utilized multiple methods to illustrate the impact of the STE-  
429 induced O<sub>3</sub>. First of all, we employed potential vorticity (PV) at 300 hPa  
430 to distinguish between stratospheric and tropospheric air masses,  
431 considering a threshold of 2 potential vorticity units (PVU) as the  
432 dynamical tropopause (Li et al., 2023; Wang et al., 2020). According to  
433 Figure 5a, a notable high value of potential vorticity (PV) was observed in  
434 eastern China, specifically spanning from the North China Plain (NCP)  
435 area to southern China. This extensive cross-regional transport area is  
436 closely associated with typhoon "Muifa" (as depicted in Figure S5). The  
437 presence of a strong anticyclone on the outer periphery of the typhoon  
438 further intensified the cross-regional transport in eastern China. This was  
439 true with the LPDM simulation, as it revealed that the PRD region was  
440 predominantly influenced by northerly air flow originating from central  
441 China (Figure S6). As a result, the potential impact of stratospheric O<sub>3</sub>  
442 intrusion on the troposphere formed a distinct and extensive band that  
443 stretched from the north to the south over eastern China. The subsequent  
444 investigations further supported this finding, as we found similar patterns,  
445 including notable high O<sub>3</sub> distribution at 300 hPa (Figure 5b), dry air  
446 (Figure 5c), and low geopotential height (Figure 5d) along the high PV area.  
447 These patterns suggested that the stratospheric intrusion did transport both



448 dry and O<sub>3</sub>-rich air masses to the troposphere. Meanwhile, the transported  
449 region exhibited a prevailing downward airflow with positive vertical  
450 velocity (Figure 5e), and a distinct high O<sub>3</sub> area was also observed along  
451 the transported band at 700 hPa (Figure 5f), indicating that the O<sub>3</sub> induced  
452 by STE could impact the lower troposphere. Similar patterns were  
453 consistently observed on other days between September 13-16, 2022  
454 (Figure S7-S9), confirming the continuous nature of the STE event.

455 The CAM-Chem model was further adopted to quantify the impact of STE-  
456 induced O<sub>3</sub>. In this model, we introduced a tracer, O<sub>3</sub>S, to represent the  
457 concentration of O<sub>3</sub> from stratosphere. Figure 6 convinced again the  
458 previous analyses that the transport of O<sub>3</sub>-rich air from the stratosphere to  
459 the troposphere, spanning from the northern to the southern China. The  
460 cross-regional transport of O<sub>3</sub>S was notable at higher levels (between  
461 500hPa and 300hPa) in the troposphere with substantial contributions  
462 exceeding 50 ppb. Though the influence reduced in the lower of the  
463 troposphere, the impacted contribution was still high. The simulated  
464 maxima of O<sub>3</sub>S at the surface level could reach up to approximately 8 ppb,  
465 indicating a non-negligible impact of STE.

466

#### 467 **4 Conclusion and implication**

468 This study adopted an integrated methodology, utilizing concurrent  
469 observations, machine learning techniques, and numerical simulations, to  
470 probe how natural processes triggered by extreme hot weather conditions  
471 (the continuous combined influence of the Subtropical High and typhoon  
472 peripheries) on O<sub>3</sub> pollution. Various natural processes, including  
473 meteorological factors, natural emissions, chemistry pathway and  
474 atmospheric transport, were investigated and summarized in Figure 7.  
475 Firstly, we found that meteorological conditions during extreme weather  
476 events, characterized by high temperatures, high pressure, and low  
477 humidity, greatly facilitated regional photochemical reaction. Through the  
478 application of machine learning techniques, we identified that  
479 meteorological factors contribute an additional 10.8 ppb to O<sub>3</sub> levels  
480 compared to the same period in previous years, with surface temperature  
481 exerting the most prominent influence. Furthermore, our investigation  
482 revealed that the hot weather stimulated BVOC emissions (increased by

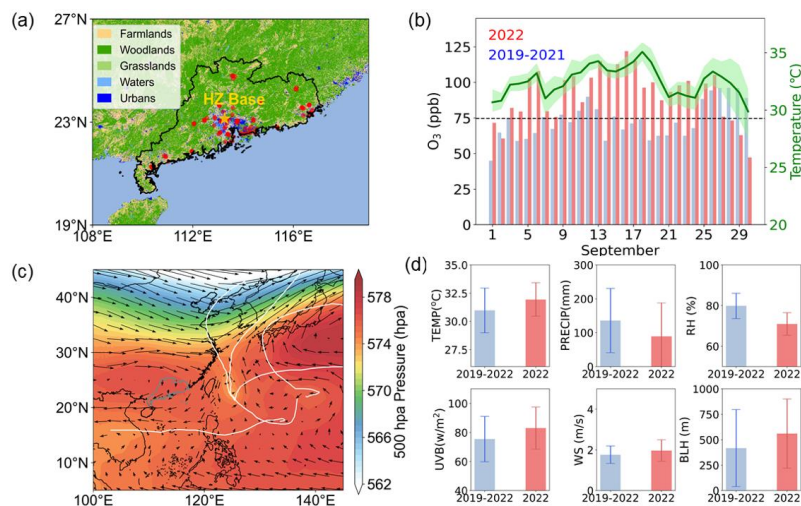


483 10%). Due to the typical high  $\text{NO}_x$  environment (mainly from  
484 anthropogenic emission) in the PRD region, BVOC emissions aggravated  
485 photochemical reaction and contributed nearly half of in-situ  $\text{O}_3$  production.  
486 The chemical transformation pathways of isoprene and its intermediate  
487 products were further explored, it was found that the further degradation of  
488 initial oxidation products of isoprene was responsible for a large fraction  
489 of isoprene contributions to  $\text{O}_3$  formation. This could be an important  
490 mechanism of isoprene affecting downwind air quality. In addition, the  
491 impact of extreme weather on atmospheric transport was also investigated.  
492 The phenomenon of STE usually takes place in high latitudes. Interestingly,  
493 we discovered that the outer periphery of a typhoon, aggravated the cross-  
494 regional transport of STE-induced  $\text{O}_3$ , spanning from the northern China  
495 to southern China. This process resulted in a non-negligible contributor to  
496 the surface levels in downwind area (such as the PRD).  
497 Our study underscores the importance of natural processes induced by  
498 extreme weather events in  $\text{O}_3$  pollution and provides valuable insights for  
499 future endeavors in  $\text{O}_3$  pollution control. Given the impact of climate  
500 change, many regions around the world are experiencing an increase in the  
501 frequency of extreme weather events, thereby intensifying natural  
502 processes. This trend is particularly notable in developed regions with high  
503 levels of anthropogenic emissions, such as eastern China, southeastern  
504 America and northern India. The interaction between natural process and  
505 human activities might further exacerbate air pollution. Future pollution  
506 control and prevention efforts should not solely focus on reducing  
507 anthropogenic emissions. Instead, a comprehensive consideration of both  
508 anthropogenic impact and natural impact should be taken into account, and  
509 a coordinated cross-regional joint emission control is highly recommended.  
510



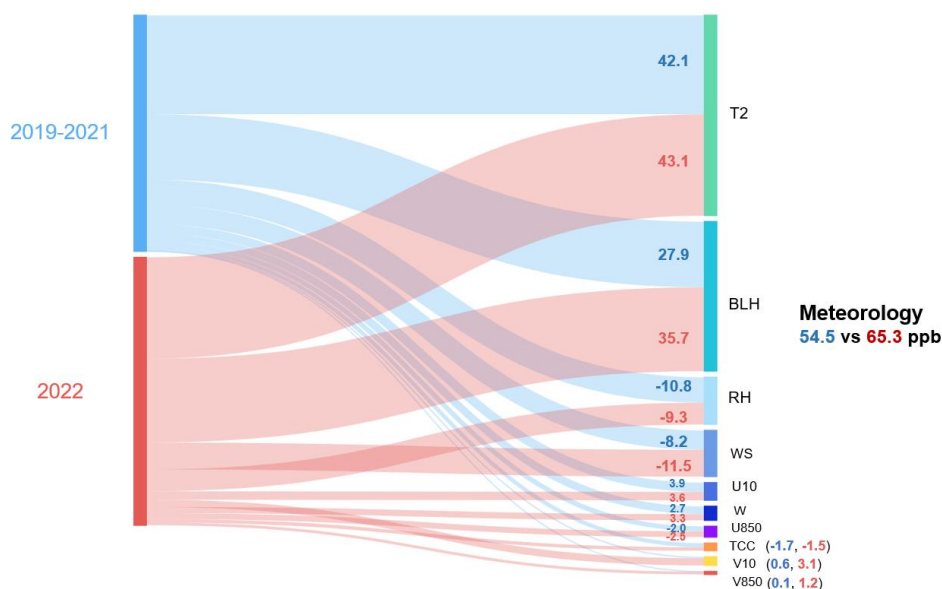


511 **List of Figures**



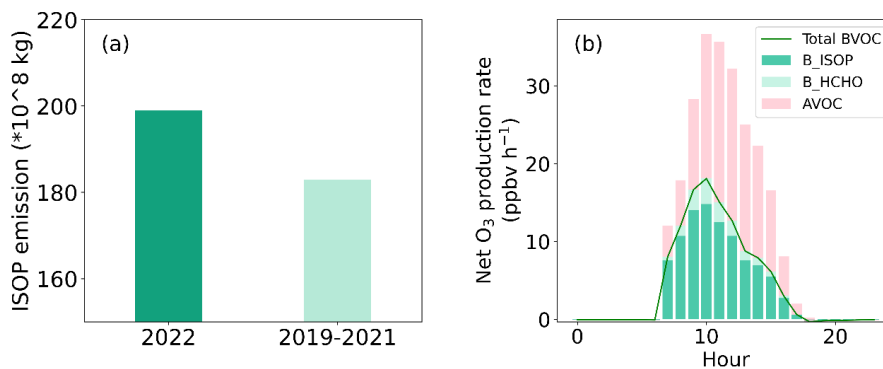
512

513 Figure 1 (a) Map showing the geographical distribution of PRD. The red dots show the air quality monitoring  
 514 network and the yellow star shows the in-situ site at Guangzhou Haizhu Urban Ecological Meteorological  
 515 Comprehensive Observation Base (HZ Base); (b) Variation of MDA8-90 O<sub>3</sub> concentrations and regional daily max  
 516 temperature (The green line shows the average, and the upper and lower shade indicate the 75<sup>th</sup> and 25<sup>th</sup> percentile,  
 517 respectively); (c) Distribution of 500 hPa pressure and winds. The white line shows the typhoon track; (d)  
 518 Comparisons of meteorological parameters between 2022 and 2019-2021



519  
 520

Figure 2 Contributions of multi-meteorological factors to O<sub>3</sub> in the September of 2022 and 2019-2021

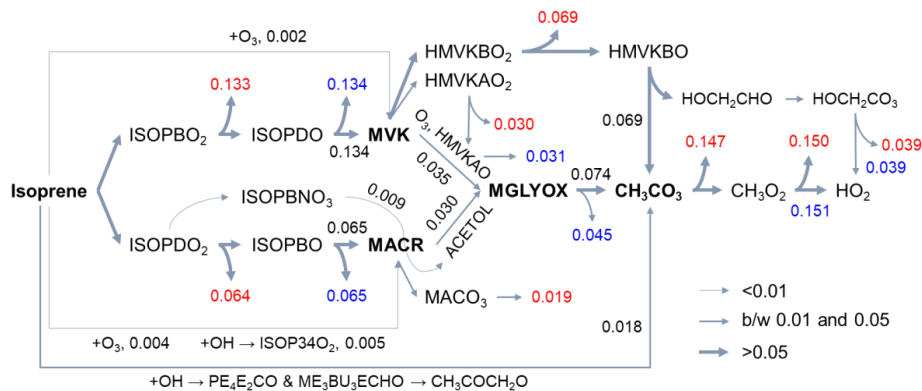


521

522 Figure 3 (a) Isoprene emissions in PRD in September in 2022 and 2019 – 2021; (b) Net OPR attributed to biogenic  
 523 isoprene (B\_ISOP), HCHO (B\_HCHO), total BVOC and anthropogenic VOC (AVOC) in September 2022.

524

525



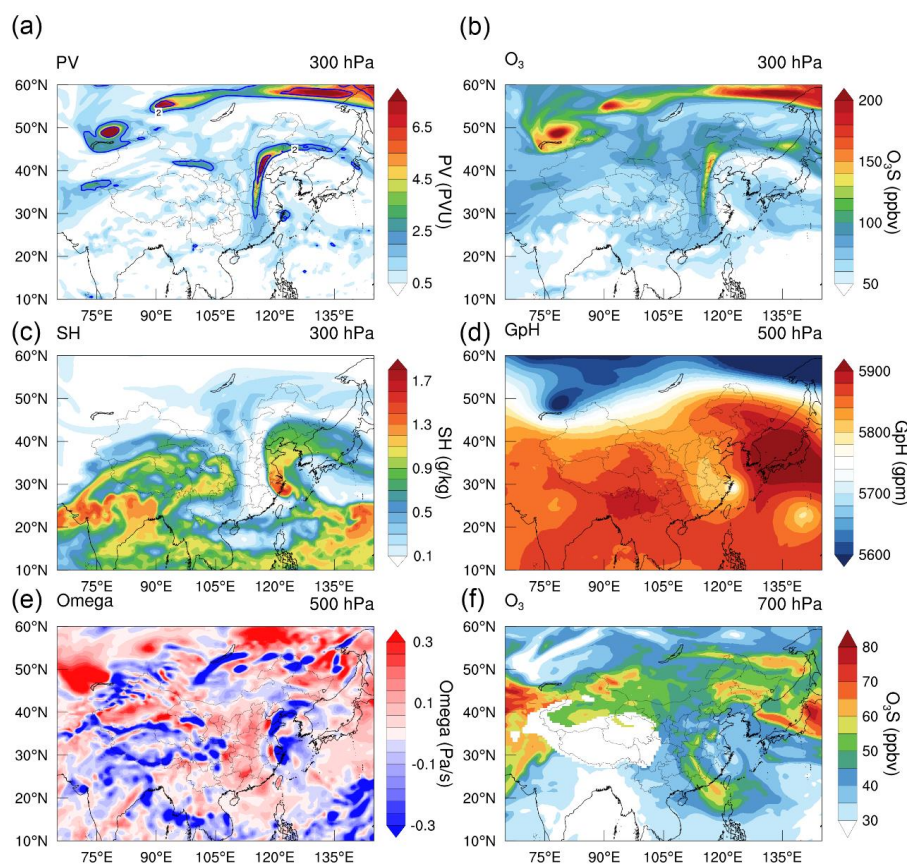
526

527 Figure 4 Changes in the rates (numbers; unit: ppbv h<sup>-1</sup>) of major reactions leading to O<sub>3</sub> formation at 12:00 induced  
 528 by 10% increase in isoprene concentrations. Red and blue fonts indicate the production rates of NO<sub>2</sub> (via RO<sub>2</sub> + NO)  
 529 and HO<sub>2</sub>, respectively. Abbreviations of the species conform to the MCM naming convention  
 530 (<http://chmlin9.leeds.ac.uk/MCMv3.3.1/home.htm>).

531

532

533



534  
535 Figure 5 Evidence illustrating STE O<sub>3</sub> intrusion on September 14, 2022. (a) Spatial distribution of potential vorticity  
536 (PV) at 300hPa over China (The blue solid line indicates the dynamical tropopause of 2PVU, 1 PVU=10<sup>-6</sup> m<sup>2</sup> s<sup>-1</sup> K  
537 kg<sup>-1</sup>); (b-e) The distribution of O<sub>3</sub> concentration (at 300 hPa), specific humidity (at 300 hPa, SH), geopotential height  
538 (at 500 hPa, Gph), vertical velocity (at 500 hPa, Omega), and O<sub>3</sub> concentration (at 700 hPa), respectively. All the  
539 data were identified based on ERA5 database.

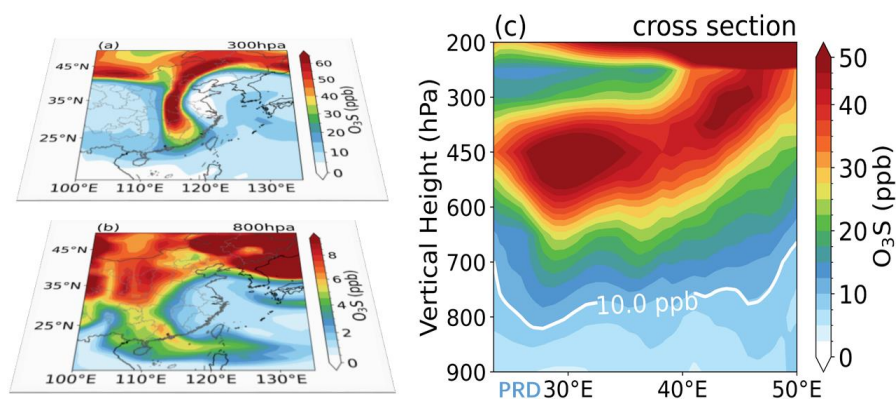
540

541

542

543

544



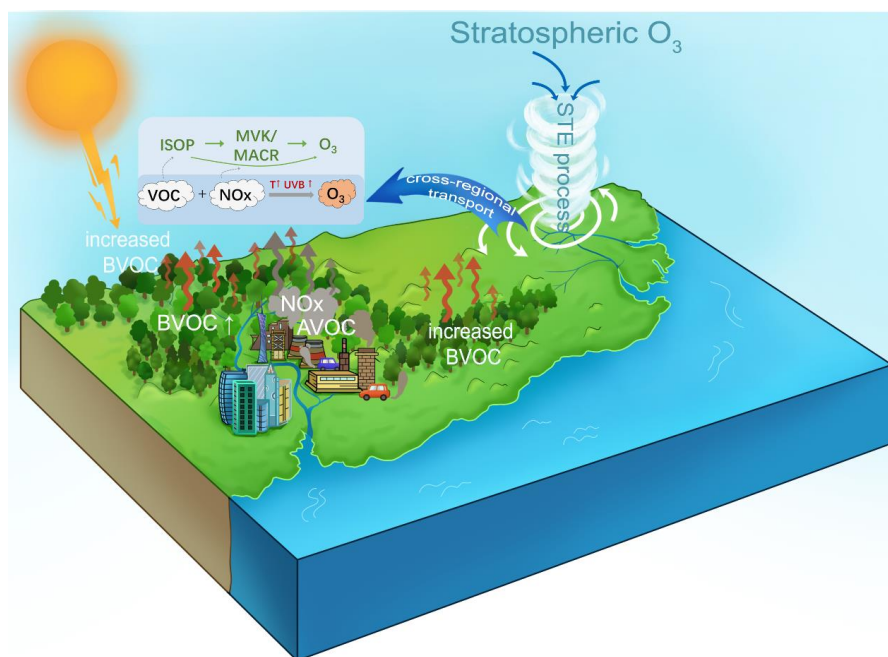
545

546 Figure 6 Distribution of CAM-chem simulated O<sub>3</sub>S. (a) O<sub>3</sub>S distribution at 300 hPa; (b) same as (a) but at 800 hPa;

547 (c) Vertical transection of O<sub>3</sub>S along the 113°E.

548

549



550

551 Figure 7 Conceptual scheme illustrating how extreme weather induced natural processes affecting O<sub>3</sub> in PRD.

552

553



554 **Associated Content (Supporting Information)**

555 Validation of the stepwise regression model(Figure S1); Synoptic weather  
556 distribution (Figure S2); LPDM simulated 48h retroplume (footprint  
557 residence time) (Figure S3); Evidence illustrating STE O3 intrusion  
558 (Figure S4-S6); Introduction of monitoring instruments (Table S1);  
559 Introduction of the recorded tropical cyclones (Table S2)

560 **Author Contributions**

561 N.W. designed the research. N.W. and X.L. wrote the manuscript. N.W. ,  
562 X.L., H.W., X.C. and F.Y. contributed to the interpretation of the results.  
563 All authors provided critical feedback and helped shape the research,  
564 analysis, and manuscript.

565 **Competing Interests**

566 The contact author has declared that none of the authors has any competing  
567 interests.

568 **Acknowledgement**

569 This study is funded by Fundamental Research Funds for the Central  
570 Universities (Grant No. YJ202313), the Guangdong Basic and Applied  
571 Basic Research Foundation (Grant No. 2022A1515011753, and  
572 2023A1515012205), the Science and Technology Research Project of  
573 Guangdong Meteorological Bureau (Grant No. GRMC2020Z06), and the  
574 Young Talent Support Project of Guangzhou Association for Science and  
575 Technology (Grant No. QT-2023-048).

576

577

578



579 **Reference**

- 580 Ashmore, M.: Assessing the future global impacts of ozone on vegetation, *Plant, Cell &*  
581 *Environment*, 28, 949-964, 2005.
- 582 Banerjee, A., Maycock, A. C., Archibald, A. T., Abraham, N. L., Telford, P., Braesicke, P., and Pyle, J.  
583 A.: Drivers of changes in stratospheric and tropospheric ozone between year 2000 and 2100,  
584 *Atmospheric Chemistry and Physics*, 16, 2727-2746, 2016.
- 585 Camalier, L., Cox, W., and Dolwick, P.: The effects of meteorology on ozone in urban areas and  
586 their use in assessing ozone trends, *Atmospheric environment*, 41, 7127-7137, 2007.
- 587 Chan, C. and Chan, L.: Effect of meteorology and air pollutant transport on ozone episodes at a  
588 subtropical coastal Asian city, Hong Kong, *Journal of Geophysical Research: Atmospheres*, 105,  
589 20707-20724, 2000.
- 590 Chen, X., Wang, N., Wang, G., Wang, Z., Chen, H., Cheng, C., Li, M., Zheng, L., Wu, L., Zhang, Q.,  
591 Tang, M., Huang, B., Wang, X., and Zhou, Z.: The Influence of Synoptic Weather Patterns on  
592 Spatiotemporal Characteristics of Ozone Pollution Across Pearl River Delta of Southern China,  
593 *Journal of Geophysical Research: Atmospheres*, 127, 10.1029/2022jd037121, 2022.
- 594 Derwent, R. G., Jenkin, M. E., Saunders, S. M., and Pilling, M. J.: Photochemical ozone creation  
595 potentials for organic compounds in northwest Europe calculated with a master chemical  
596 mechanism, *Atmospheric environment*, 32, 2429-2441, 1998.
- 597 Ding, A., Huang, X., and Fu, C.: Air pollution and weather interaction in East Asia, in: *Oxford*  
598 *Research Encyclopedia of Environmental Science*, 2017.
- 599 Eyring, V., Arblaster, J. M., Cionni, I., Sedláček, J., Perlwitz, J., Young, P. J., Bekki, S., Bergmann, D.,  
600 Cameron-Smith, P., and Collins, W. J.: Long-term ozone changes and associated climate impacts  
601 in CMIP5 simulations, *Journal of Geophysical Research: Atmospheres*, 118, 5029-5060, 2013.
- 602 Gao, D., Xie, M., Liu, J., Wang, T., Ma, C., Bai, H., Chen, X., Li, M., Zhuang, B., and Li, S.: Ozone  
603 variability induced by synoptic weather patterns in warm seasons of 2014–2018 over the Yangtze  
604 River Delta region, China, *Atmospheric Chemistry and Physics*, 21, 5847-5864, 2021.
- 605 Gaudel, A., Cooper, O. R., Ancellet, G., Barret, B., Boynard, A., Burrows, J. P., Clerbaux, C., Coheur,  
606 P.-F., Cuesta, J., and Cuevas, E.: Tropospheric Ozone Assessment Report: Present-day distribution  
607 and trends of tropospheric ozone relevant to climate and global atmospheric chemistry model  
608 evaluation, *Elementa: science of the anthropocene*, 6, 2018.
- 609 Guenther, A., Jiang, X., Heald, C. L., Sakulyanontvittaya, T., Duhl, T. a., Emmons, L., and Wang, X.:  
610 The Model of Emissions of Gases and Aerosols from Nature version 2.1 (MEGAN2. 1): an extended  
611 and updated framework for modeling biogenic emissions, *Geoscientific Model Development*, 5,  
612 1471-1492, 2012.
- 613 Han, H., Liu, J., Shu, L., Wang, T., and Yuan, H.: Local and synoptic meteorological influences on  
614 daily variability in summertime surface ozone in eastern China, *Atmospheric Chemistry and Physics*,  
615 20, 203-222, 2020.
- 616 Jacob, D. J.: Heterogeneous chemistry and tropospheric ozone, *Atmospheric Environment*, 34,  
617 2131-2159, 2000.
- 618 Jenkin, M. E. and Clemitshaw, K. C.: Ozone and other secondary photochemical pollutants:  
619 chemical processes governing their formation in the planetary boundary layer, *Atmospheric*  
620 *Environment*, 34, 2499-2527, 2000.
- 621 Johnsson, T.: A procedure for stepwise regression analysis, *Statistical Papers*, 33, 21-29, 1992.
- 622 Knowlton, K., Rosenthal, J. E., Hogrefe, C., Lynn, B., Gaffin, S., Goldberg, R., Rosenzweig, C., Civerolo,



- 623 K., Ku, J.-Y., and Kinney, P. L.: Assessing ozone-related health impacts under a changing climate,  
624 Environmental health perspectives, 112, 1557-1563, 2004.
- 625 Lei, Y., Yue, X., Liao, H., Zhang, L., Zhou, H., Tian, C., Gong, C., Ma, Y., Cao, Y., and Seco, R.: Global  
626 perspective of drought impacts on ozone pollution episodes, Environmental science & technology,  
627 56, 3932-3940, 2022.
- 628 Li, T., Wu, N., Chen, J., Chan, P.-w., Tang, J., and Wang, N.: Vertical exchange and cross-regional  
629 transport of lower-tropospheric ozone over Hong Kong, Atmospheric Research, 292, 106877,  
630 10.1016/j.atmosres.2023.106877, 2023.
- 631 Lu, X., Zhang, L., and Shen, L.: Meteorology and Climate Influences on Tropospheric Ozone: a  
632 Review of Natural Sources, Chemistry, and Transport Patterns, Current Pollution Reports, 5, 238-  
633 260, 10.1007/s40726-019-00118-3, 2019.
- 634 Lu, X., Hong, J., Zhang, L., Cooper, O. R., Schultz, M. G., Xu, X., Wang, T., Gao, M., Zhao, Y., and  
635 Zhang, Y.: Severe surface ozone pollution in China: a global perspective, Environmental Science &  
636 Technology Letters, 5, 487-494, 2018.
- 637 Lyu, X., Guo, H., Zou, Q., Li, K., Xiong, E., Zhou, B., Guo, P., Jiang, F., and Tian, X.: Evidence for  
638 Reducing Volatile Organic Compounds to Improve Air Quality from Concurrent Observations and  
639 In Situ Simulations at 10 Stations in Eastern China, Environmental Science & Technology, 56,  
640 15356-15364, 2022.
- 641 Lyu, X., Wang, N., Guo, H., Xue, L., Jiang, F., Zeren, Y., Cheng, H., Cai, Z., Han, L., and Zhou, Y.:  
642 Causes of a continuous summertime O<sub>3</sub> pollution event in Jinan, a central city in the North China  
643 Plain, Atmospheric Chemistry and Physics, 19, 3025-3042, 2019.
- 644 Pierotti, D., Wofsy, S., Jacob, D., and Rasmussen, R.: Isoprene and its oxidation products:  
645 Methacrolein and methyl vinyl ketone, Journal of Geophysical Research: Atmospheres, 95, 1871-  
646 1881, 1990.
- 647 Pusede, S. E., Steiner, A. L., and Cohen, R. C.: Temperature and recent trends in the chemistry of  
648 continental surface ozone, Chemical reviews, 115, 3898-3918, 2015.
- 649 Stohl, A., Bonasoni, P., Cristofanelli, P., Collins, W., Feichter, J., Frank, A., Forster, C., Gerasopoulos,  
650 E., Gäggeler, H., and James, P.: Stratosphere-troposphere exchange: A review, and what we have  
651 learned from STACCATO, Journal of Geophysical Research: Atmospheres, 108, 2003.
- 652 Wang, H., Wang, W., Shangguan, M., Wang, T., Hong, J., Zhao, S., and Zhu, J.: The Stratosphere-  
653 to-Troposphere Transport Related to Rossby Wave Breaking and Its Impact on Summertime  
654 Ground-Level Ozone in Eastern China, Remote Sensing, 15, 2647, 10.3390/rs15102647, 2023.
- 655 Wang, N., Huang, X., Xu, J., Wang, T., Tan, Z.-m., and Ding, A.: Typhoon-boosted biogenic emission  
656 aggravates cross-regional ozone pollution in China, Science Advances, 8, eabl6166, 2022.
- 657 Wang, N., Lyu, X., Deng, X., Huang, X., Jiang, F., and Ding, A.: Aggravating O<sub>3</sub> pollution due to  
658 NO<sub>x</sub> emission control in eastern China, Science of the Total Environment, 677, 732-744, 2019.
- 659 Wang, T., Xue, L., Brimblecombe, P., Lam, Y. F., Li, L., and Zhang, L.: Ozone pollution in China: A  
660 review of concentrations, meteorological influences, chemical precursors, and effects, Science of  
661 the Total Environment, 575, 1582-1596, 2017.
- 662 Wang, Y., Wang, H., and Wang, W.: A stratospheric intrusion-influenced ozone pollution episode  
663 associated with an intense horizontal-trough event, Atmosphere, 11, 164, 2020.
- 664 Westerling, A. L., Hidalgo, H. G., Cayan, D. R., and Swetnam, T. W.: Warming and earlier spring  
665 increase western US forest wildfire activity, science, 313, 940-943, 2006.
- 666 Wolfe, G. M., Marvin, M. R., Roberts, S. J., Travis, K. R., and Liao, J.: The framework for O-D



667 atmospheric modeling (F0AM) v3. 1, Geoscientific Model Development, 9, 3309-3319, 2016.  
668 Yue, X. and Unger, N.: Fire air pollution reduces global terrestrial productivity, Nature  
669 Communications, 9, 5413, 2018.

670

671